UNIVERSITY OF CALIFORNIA, SAN DIEGO

Patient-specific Modeling of Cardiac Biomechanics in Repaired Tetralogy of Fallot

A Thesis submitted in partial satisfaction of the requirements
for the degree Master of Science

in

Bioengineering

by

Cherilyn Tongohan Go

Committee in charge:

Jeffrey H. Omens, Chair
Andrew D. McCulloch, Co-Chair
Pedro J. Cabrales Arevalo
Sanjeet R. Hegde

2016

The Thesis of Cherilyn Tongohan Go is approved and it is acceptable in quality and form for publication on microfilm and electronically:

_____

_____

_____
Co-Chair

_____
Chair

University of California, San Diego

2016

DEDICATION

I dedicate this thesis to my family, for always being my greatest support system. To my parents especially—this already goes without saying, but I love you two for being the most selfless parents and for always making sure that my happiness and health are a priority. You two have shown me, in the humblest of ways, how to be strong, how to work hard, how to be respectful, and above all, how to love. Now that I'm done with all these (seemingly endless) years of school, I hope that I can begin to provide for the two of you so as you've always provided for me so that you can finally put your own happiness and health first.

TABLE OF CONTENTS

LIST OF ABBREVIATIONS

2D	Two-dimensional
3D	Three-dimensional
AV	Atrio-ventricular
EDP	End-diastolic pressure
EDV	End-diastolic volume
EDPVR	End-diastolic pressure-volume relation
ESP	End-systolic pressure
ESV	End-systolic volume
ESVI	End-systolic volume index
LV	Left ventricle
MR	Magnetic resonance
PA	Pulmonary artery
PR	Pulmonary regurgitation
PVR	Pulmonary valve replacement
RV	Right ventricle
RVEDVI	Right ventricular end-diastolic volume index
RVFW	Right ventricular free wall
RVOTO	Right ventricular outflow tract obstruction
ToF	Tetralogy of Fallot
TPV	Transcatheter pulmonary valve
VSD	Ventricular septal defect

LIST OF FIGURES

LIST OF TABLES

ABSTRACT OF THE THESIS

Patient-specific Modeling of Cardiac Biomechanics in Repaired Tetralogy of Fallot

by

Cherilyn Tongohan Go

Master of Science in Bioengineering

University of California, San Diego, 2016

Jeffrey H. Omens, Chair
Andrew D. McCulloch, Co-Chair

Surgical advancements in the management of Tetralogy of Fallot, the most common cyanotic congenital heart defect, have allowed individuals to survive into adulthood. However, most individuals develop pulmonary regurgitation, causing right ventricular volume overload, dilatation, and possible dysfunction. These patients require pulmonary valve replacement (PVR), but the timing and indications for the operation are still under investigation. One proposed clinical indicator for PVR is a right ventricular

end-diastolic volume index (RVEDVI) greater than 150 mL/m^2, though this threshold value is somewhat controversial. Because diastolic fiber strains have been found to correlate well with ventricular remodeling in response to volume overload, a correlation may also exist between diastolic fiber strain and reverse remodeling after alleviation of volume overload. In this thesis, biventricular image-based computational models were developed to test the hypothesis that RVEDVI correlates with post-PVR regional diastolic fiber strains in the right ventricle. Two computational models with RVEDVIs of 170 mL/m^2 and 115 mL/m^2 were developed, and each model underwent full-beat simulation before and after virtual PVR. Preliminary findings suggest that RVEDVI may in fact correlate negatively with post-PVR regional diastolic fiber strains of repaired ToF patients, particularly in regions of the right ventricular free wall adjacent to the septum.

Chapter 1: Background

1.1 Cardiac Anatomy & Physiology

The heart is a muscular organ that relies on the complex interaction of multiple components—passive material properties, active contractile properties, geometry, hemodynamic loading conditions, electrical activation, and neurohumoral stimulation—to effectively pump blood throughout the extensive network of arteries, veins, and capillaries that make up the cardiovascular system. The cardiovascular system is comprised of two circuits: the pulmonary circuit, which is responsible for delivering deoxygenated blood from the right side of the heart to the lungs and returning the newly oxygenated blood to the left side of the heart, and the systemic circuit, which is responsible for delivering oxygenated blood from the left side of the heart to all other organs of the body and returning the deoxygenated blood back to the right side of the heart.

Being the central hub of the cardiovascular system, the heart consists of two upper chambers—the right and left atria—responsible for collecting blood and two muscular lower chambers—the right and left ventricles—responsible for pumping blood out for delivery to the body. Uni-directional blood flow through each side of the heart is tightly regulated by the coordinated opening and closing of both the atrioventricular (AV) valves and the semilunar valves. AV valves regulate blood flow between the atria and ventricles, while semilunar valves regulate blood flow between the ventricles and their respective outflow tracts. In the right heart, the tricuspid valve is the AV valve and the pulmonary valve is the semilunar valve. In the left heart, the mitral valve is the AV valve and the aortic valve is the semilunar valve.

1.2 Cardiac Muscle Architecture

The heart wall is composed of three distinct layers: a thin endothelial layer lining the inside of the atria and ventricles called the endocardium, a thick muscular layer called the myocardium, and a double walled outer membrane called the pericardium.

The cardiac muscle cells found in the myocardium are called cardiomyocytes, or myofibers. Each cardiomyocyte is composed of bundles of myofibrils, and is consequently long and cylindrical in shape, measuring approximately 17-25 um in diameter and 60-140um in length [1]. At the tissue scale, these myofibers are organized into laminar sheets, with fiber and sheet orientations varying throughout the ventricular walls [2]. The fibrous architecture of the myocardium lends significantly to the anisotropy of electrophysiological and biomechanical behavior that dictate the heart's functionality.

1.3 Cardiac Cycle

The cardiac cycle is divided into the diastolic (passive filling) phase and systolic (active contraction) phase. Diastole can be further divided into mid-late diastole and early diastole, and systole can been divided into isovolumetric contraction and ventricular ejection. As stated previously, unidirectional blood flow through the heart is achieved by the coordinated opening and closing of the AV and semilunar valves. The state of each valve is determined by the pressure difference across them. During mid-to-late diastole, atrial pressures are greater than ventricular pressures, causing the AV valves to remain open while the ventricles fill with blood. During late diastole, the atria contract, causing a slight bump in both atrial and ventricular pressure. As atrial pressures drop below ventricular pressures at the end of diastole/beginning of systole, the AV valves close. While both AV and semilunar valves are closed, the ventricles undergo isovolumetric contraction. At this point of the cardiac cycle, ventricular

contraction causes ventricular pressures to increase beyond the pressure of the aorta and pulmonary artery, causing the semilunar valves to open and blood to flow out from the ventricles to their respective outflow tracts, a phase known as ventricular ejection. As the ventricular pressures decrease, the higher pressures in the aorta and pulmonary artery cause the semilunar valves to close. With all valves closed again, the ventricles undergo isovolumetric relaxation. As atrial pressures climb above ventricular pressures, the AV valves open, the ventricles fill passively, and the cardiac cycle starts again from the beginning.

1.4 Tetralogy of Fallot

1.4.1 Definition

Congenital heart defects, the most common type of birth defect, are anomalies in cardiac structure present at birth. These defects range in complexity and severity, and some individuals are born with a combination of defects. The most common form of cyanotic congenital heart defect is Tetralogy of Fallot (ToF), affecting approximately 3 of every 10,000 live births [1]. ToF is defined by a combination of four structural anomalies in the heart (Figure 1.1):

1) a ventricular septal defect (VSD)
2) an overriding aorta
3) right ventricular outflow tract obstruction (RVOTO), and
4) right ventricular hypertrophy.

Like many congenital heart defects, the exact cause of ToF is still under investigation. However, recent studies have demonstrated that the general phenotype of ToF may be associated with chromosomal anomalies such as trisomy 13 and trisomy 21 and microchromosomal anomalies such as 22q11.2 deletion [3]. Presentation of ToF

sub-phenotypes in individuals with these different genetic mutations suggests that each genetic mutation may have a different pathogenetic mechanism for causing the phenotypic defects that are generally classified as ToF.

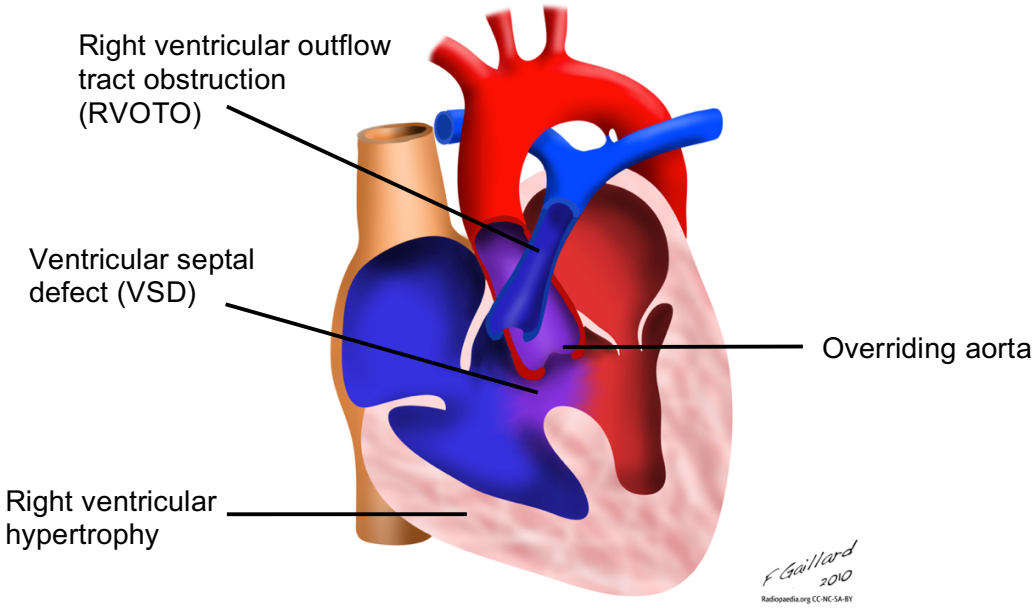

Figure 1.1: Illustration of ToF anatomy. (Source: Dr. Frank Gaillard, Radiopadia.org; rID:8488 2016) [5].

1.4.2 ToF Anatomy and Pathophysiology

Though ToF is described by the presence of the four structural anomalies stated in the previous section, the landmark of ToF is the malalignment of the abnormally extensive outlet septum with respect to the remainder of the ventricular septum [3]. This single deviation from normal cardiac anatomy results in the formation of a VSD, overriding aorta, and RVOTO. Hypertrophy of the right ventricle develops shortly after birth as a compensatory hemodynamic response to the presence of the first three anomalies. Each of ToF's four structural anomalies contribute to the improper functioning of the right heart and is described in further detail below.

The first structural anomaly, the VSD, is a hole in the septal wall that separates the right and left ventricles. Because pressure in the left ventricle is greater than that in

the right ventricle, especially during systole, the presence of a VSD allows the free flow of blood from the high pressure left ventricle to the low pressure right ventricle. VSDs range in size and severity among individuals, with a larger hole allowing a greater amount of shunting. An excessive increase in right ventricular pressure, and consequently an excessive increase in pulmonary blood flow, may lead to the development of pulmonary hypertension or reversal of blood flow at the pulmonary valve.

The second structural anomaly is the overriding aorta, a defect in which the aorta is positioned directly above the VSD and receives blood from both ventricles rather than just the left ventricle. Therefore, instead of carrying solely oxygen-rich blood to the systemic circuit, the aorta carries a mixture of oxygen-poor blood from the right ventricle and oxygen-rich blood from the left ventricle, effectively reducing the rate of oxygen delivery to systemic tissues. Left untreated, the lack of sufficient oxygen may lead to organ failure.

The third structural anomaly, RVOTO, is characterized by the degree and location of the obstruction. In less mild to moderate cases, the RVOT is narrowed, or stenotic; in severe cases, the RVOT demonstrates complete obstruction, or atresia. The RVOTO can be found in any of three locations, each with respect to the pulmonary valve: the subvalvular region of the tract (due to a thickened muscular infundibulum), at the pulmonary valve, or in the supravalvular region of the tract [3]. This structural defect reduces blood flow to the lungs and causes the right ventricle to work harder in efforts to compensate for the reduction of pulmonary blood flow.

The fourth and final structural anomaly is right ventricular hypertrophy. This defect is defined by the thickening of the right ventricular walls as an adaptive response to the increased workload, which in turn is a response to the first three structural defects.

As the walls thicken, their compliance decreases; this progressive contractile dysfunction causes the right ventricle to dilate to provide a compensatory preload and an increase in compliance. The enlarged right ventricle has thin, weak walls and may no longer pump enough blood to meet the needs of the body. Thus, if left untreated, right ventricular hypertrophy may lead to congestive right heart failure. Additionally, an increase in RV size also increases the risk for ventricular arrhythmia and sudden death.

1.5 ToF Treatment

Most commonly, TOF patients undergo complete intracardiac repair during the first 3 to 11 months of age. The goal of surgery is to close the VSD and relieve RVOTO. In the past, an extensive incision of the right ventricular free wall was used to access the intracardiac region of interest. The VSD was closed by suturing a Dacron patch over the septal hole. RVOTO was completely relieved by making a large incision across the pulmonary valve annulus and placing a transannular patch to widen the annulus. Though complete RVOTO relief was easily accomplished with this approach, the right ventriculotomy and transannular patch resulted in severe late complications such as pulmonary regurgitation, myocardial scarring, and increased risk of ventricular tachycardia and sudden death [5].

Since about 30 years ago, surgical planning for intracardiac repair has shifted towards a more conservative approach that aims to preserve the integrity of the right ventricle (RV) and pulmonary valve. In order to access the intracardiac region of interest, either a single incision is made in the right atrium or a double incision is made in the right atrium and pulmonary artery, rather than an extensive ventriculotomy. The VSD is closed by suturing a Dacron patch over the affected area.

In cases of RVOTO for which obstruction is localized to the subvalvular or supravalvular region, and in cases of mild stenosis at the valve, both the RV and pulmonary valve remain intact. Relief is achieved by the resection of an obstructing muscular bundle in the subvalvular region, a balloon valvuloplasty at the valve, or the placement of a nontransannular patch in the supravalvular region [3]. In moderate-severe cases of RVOTO at the valve, the RV remains intact but the integrity of the pulmonary valve is compromised for the placement of a transannular patch (Figure 1.2, left). In severe cases in which the pulmonary valve is extremely narrow or pulmonary atresia is present, incisions are made in the pulmonary artery and right ventricle for the placement of a right ventricle-to-pulmonary artery (RV-PA) valved conduit (Figure 1.2, right). This conduit replaces the pulmonary valve and allows sufficient blood flow to the lungs.

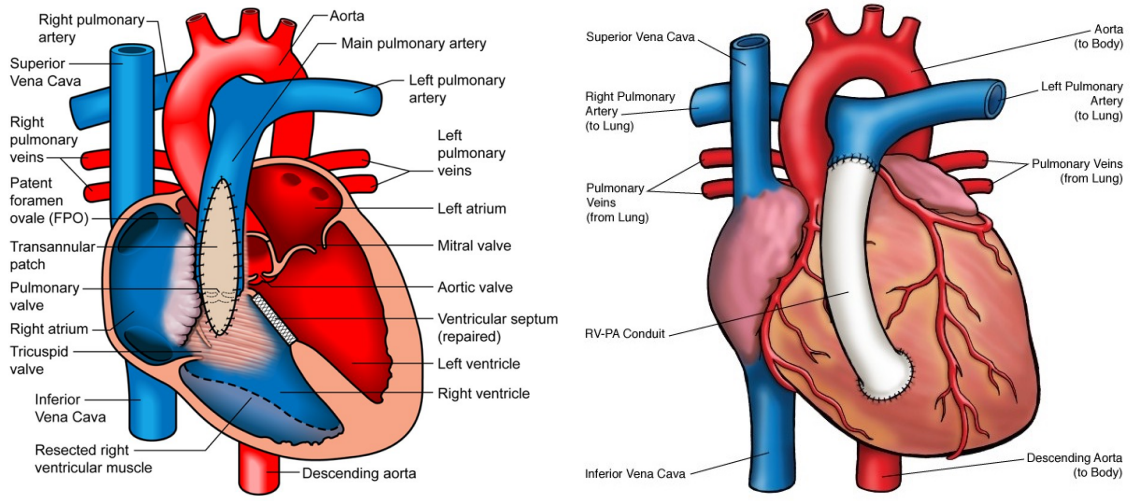

Figure 1.2: Illustration of Tetralogy of Fallot repair using a transannular patch (left) and a right ventricle-to-pulmonary artery (RV-PA) conduit (right). Source: *Tetralogy of Fallot Repair* 2014 [7].

1.6 Late Complications of ToF Repair

Surgical repair of ToF has been reported to have excellent long-term outcomes, with a survival rate of 86% at 30 years after primary repair [8]. Nevertheless, postoperative complications are expected, and individuals must have lifelong follow-up examinations.

1.6.1 Pulmonary Regurgitation

The most common late complication of ToF repair is pulmonary regurgitation (PR), which occurs when an incompetent pulmonary valve is present, causing blood to flow back into the RV. In individuals who received a transannular patch during primary repair, progressive transannular patch enlargement causes the pulmonary valve to become more dysfunctional over time, leading to the development of PR. In individuals who received a RV-PA conduit, multiple factors such as calcification, external compression, and kinking contribute to the relatively quick deterioration of the conduit, resulting in a stenotic and/or regurgitant conduit [9].

1.6.2 Right Ventricular Dilatation

Chronic RV volume overload due to PR, or chronic RV pressure overload due to pulmonary stenosis, results in RV dilatation. Generally, RV dilatation is well-tolerated in the first few years of complete repair, and RV function remains normal. However, without repair of the pulmonary valve, the RV becomes dysfunctional and the patient may develop exercise intolerance. Additionally, this increase in RV size often results in an increase in QRS duration, risk of arrhythmia, and decreased LV function (primarily a reduction of LV preload due to severe PR and worsening RV function) [6].

In chronic volume overload, RV preload is elevated. This increase causes the RV to remodel through eccentric hypertrophy, adding sarcomeres in series and increasing the RV volume. Studies in volume overloaded rats have shown that this eccentric hypertrophy may occur as a compensatory effect to normalize diastolic fiber strains [10]. Though diastolic fiber strains may play a significant role in volume overloaded remodeling, there is not much data to show the role of diastolic fiber strains in reverse remodeling after volume overloading has been alleviated. Due to this lack of knowledge, the mechanisms of reverse remodeling in repaired ToF patients after repair of their pulmonary valve remain unclear.

A study by Gerdes (2002) in volume overloaded rats found that, much like the addition of sarcomeres in series during eccentric hypertrophy, alleviation of volume overloading resulted in reverse remodeling through the reduction of sarcomeres in series [11]. One potential mechanism of reverse remodeling in the volume overloaded RV may simply be the inverse of forward remodeling—namely, the removal of sarcomeres in series as a compensatory effect to normalize below-average diastolic fiber strains. Consequently, this thesis takes a step towards understanding the mechanism of reverse remodeling by developing computational models to evaluate diastolic fiber strains in the dilated RV of a repaired ToF patient directly after pulmonary valve repair.

1.6.3 Pulmonary Valve Replacement and Timing Considerations

Pulmonary valve replacement (PVR) is the only viable option to stabilize or even reverse the deleterious effects of PR. Though PVR is an unavoidable operation for most repaired ToF individuals, it is not always effective in normalizing RV size and function, and it does not come without an increased risk for re-operation. Ideally, PVR should be delayed as much as possible to reduce the number of open-heart operations in the

individual's lifetime, but should be performed before RV dilatation and dysfunction becomes irreversible. Therefore, a significant amount of research effort in ToF management is dedicated to finding the optimal timing for PVR with respect to well-defined, consistent clinical metrics.

Recently, a less invasive operation has become available for the transcatheter delivery of a pulmonary valve in patients with dysfunctional (stenotic/regurgitant) RV-PA valved conduits. The Medtronic Melody transcatheter pulmonary valve (TPV) is a bovine jugular vein valve sutured within a platinum iridium frame that aims to restore pulmonary valve competence and prolong an existing conduit's life span [12]. Though the operation is much less invasive, it does not replace open-heart surgery and only delays the need for the next open-heart operation. Additionally, the operation is not an available option for the majority of ToF patients, many of whom have a dysfunctional native RVOT or an RVOT augmented with a transannular patch rather than an RV-PA conduit. Though the operation itself has low associated risk in comparison to surgical PVR, the same timing considerations as surgical PVR should be taken to provide individuals with the maximum amount of time free of the need for an open-heart operation. Thus, surgical PVR is performed in individuals that require a replacement valve (and do not have an existing conduit) or in individuals that require a replacement conduit, while Melody TPV implantation is only performed in individuals who have an already existing RV-PA conduit.

A few studies have elucidated possible indicators for the timing of PVR. Though similarities were found among some of the studies, there has been no unanimous agreement, and timing of the operation remains controversial. According to the editorial "Indications for Pulmonary Valve Replacement in Repaired Tetralogy of Fallot" published in *Circulation* 2013, there are several possible recommendations for the indications of

PVR in patients with repaired ToF and moderate or severe PR, as shown in Table 1 below [13].

Table 1.1: Proposed Indications for PVR in Patients With Repaired TOF or Similar Physiology With Moderate or Severe PR (Regurgitation Fraction >25%). *Reprinted with permission from “Indications for pulmonary valve replacement in repaired tetralogy of Fallot: the quest continues" by Tal Geva, 2013. Circulation, 128.17, 1855-1857 [13].

Indications	Supporting References
I. Asymptomatic patients with ≥2 of the following criteria:	
a. RV end-diastolic volume index >150 mL/m^2 or *z* score >4. In patients whose body surface area falls outside published normal data: RV/LV end-diastolic volume ratio >2	10, 12
b. RV end-systolic volume index >80 mL/m^2	11, 13
c. RV ejection fraction <47%	11, 15, 16
d. LV ejection fraction <55%	11, 15, 16
e. Large RVOT aneurysm	17, 18
f. QRS duration >160 ms	11
g. Sustained tachyarrhythmia related to right-sided heart volume load	6
h. Other hemodynamically significant abnormalities:	
• RVOT obstruction with RV systolic pressure ≥0.7 systemic	19
• Severe branch pulmonary artery stenosis (<30% flow to affected lung) not amenable to transcatheter therapy	
• Greater than or equal to moderate tricuspid regurgitation	19
• Left-to-right shunt from residual atrial or ventricular septal defects with pulmonary-to-systemic flow ratio ≥1.5	19
• Severe aortic regurgitation	19
II. Symptomatic patients fulfilling ≥1 of the quantitative criteria detailed above. Examples of symptoms and signs include:	
a. Exercise intolerance not explained by extracardiac causes (eg, lung disease, musculoskeletal anomalies, genetic anomalies, obesity), with documentation by exercise testing with metabolic cart (≤70% predicted peak $\dot{V}o_2$ for age and sex not explained by chronotropic incompetence)	
b. Signs and symptoms of heart failure (eg, dyspnea with mild effort or at rest not explained by extracardiac causes, peripheral edema)	19
c. Syncope attributable to arrhythmia	
III. Special considerations:	
a. Because of higher risk of adverse clinical outcomes in patients who underwent TOF repair at ≥3 years of age, PVR may be considered if they fulfill ≥1 of the quantitative criteria in section I	16
b. Women with severe PR and RV dilatation or dysfunction may be at risk for pregnancy-related complications. Although no evidence is available to support benefit from prepregnancy PVR, the procedure may be considered if fulfilling ≥1 of the quantitative criteria in section I	20

LV indicates left ventricular; PR, pulmonary regurgitation; PVR, pulmonary valve replacement; RV, right ventricular; RVOT, right ventricular outflow tract; and TOF, tetralogy of Fallot.

Because the indications for PVR remain controversial, a mechanistic understanding of the currently proposed clinical indicators may provide clarity for timing of the operation. For example, an RV end-diastolic volume index (EVEDVI), or RVEDV normalized to the individual's body surface area, greater than 150 mL/m^2 is commonly used as an indicator for PVR, but one study by Frigiola et al. suggested that a more aggressive approach of performing PVR at an RVEDVI less than 150 mL/m^2 may lead to better normalization of RV size [14]. Despite the controversy on which exact threshold value to use clinically, clinicians are in general agreement that the degree of RV reverse remodeling seems to be RVEDVI-dependent. The mechanism that explains the correlation between RVEDVI and the degree of reverse remodeling, however, remains unclear.

In this thesis, the development of computational models allows us to take a preliminary look into whether RVEDVI may correlate with diastolic fiber strains, and in turn, whether RVEDVI may correlate with reverse remodeling. Therefore, comparisons of the post-PVR diastolic fiber strains in models of various RVEDVIs may provide a mechanistic understanding of the differences in RV reverse remodeling at various RVEDVIs. If reverse remodeling is assumed to occur as the inverse of forward remodeling, it is first necessary to gain an adequate understanding of current research on the forward remodeling in repaired ToF.

1.7 Computational Modeling in Repaired Tetralogy of Fallot

1.7.1 Statistical Shape Models of Repaired ToF

Recent computational models of repaired ToF have focused on the statistical shape analysis of the remodeled RV, using principal component analysis to determine statistically different shape modes. A 2008 shape analysis by Sheehan et al. showed

that RV shape in repaired TOF differed from that of normal individuals in several distinct ways rather than in a shape continuum [15]. The RV exhibited a greater cross-sectional area, a rounder cross-sectional shape (free wall bulging), a lower ratio of interventricular septum surface area/total RV surface area, a flatter septal wall, and a bulging basal to the tricuspid valve when compared to normal individuals.

In another shape analysis study, published in 2013 by Leonardi et al., statistical shape modeling was used to compare the shape of repaired ToF in patients with various degrees of PR rather than comparing to normal hearts [16]. In this study, a strong correlation was found between PR severity and the degree of RV dilatation, as well as a correlation with the degree of outflow tract bulging and apical dilatation. In this way, computational modeling has begun to correlate clinical metrics, such as PR, to changes in RV shape.

Though neither of the previously mentioned studies investigated diastolic fiber strains, the knowledge that dilatation correlates with increased diastolic fiber strains and that the dilated RV of repaired ToF patients exhibited distinct shape modes suggests the idea that forward RV remodeling in repaired ToF patients may correlate with regional diastolic fiber strains rather than global diastolic fiber strains. In the same manner, RV reverse remodeling may also correlate with regional diastolic fiber strains.

1.7.2 Finite-element Modeling

Though statistical shape analysis has provided great insight into RV shape changes in patients with repaired ToF, it does not provide any insight into the mechanisms for RV remodeling and reverse remodeling. In recent years, the field of patient-specific modeling has emerged due to its ability to simulate complex systems such as the heart. Once validated, these patient-specific models have the potential for

predictive power; thus, they can provide guidance to clinicians by simulating various treatment plans and surgical interventions. With respect to our interest in repaired ToF, patient-specific computational models allow us to simulate the surgical intervention of PVR and at the same time evaluate regional diastolic fiber strains in models with various RVEDVIs.

Previous patient-specific computational models of repaired ToF patients have been developed by Tang, et. al (2010) to study the effect of patch size and degree of scar resection during PVR on RV function (i.e., stroke volume and ejection fraction) [18]. These models incorporated RV-LV, RV-patch, and fluid-structure interactions to test the hypothesis that a smaller patch and more aggressive scar resection during PVR may lead to improved RV function and reduced stress and strain near the patch. Preliminary results of the study suggested that their hypothesis may be correct. However, these models had various limitations; namely, LV blood flow, valve mechanics, and active contraction models were not included.

Because the aim of this thesis is to evaluate strains in repaired ToF patients with severe PR, the role of hemodynamics in repaired ToF patients is extremely significant, and models appropriate for this study would need to include a biventricular geometry coupled to a closed-loop circulation model that can simulate PR. Consequently, the models used in this thesis incorporate biventricular mechanics with lumped-parameter components of systemic and pulmonary circulation in a closed-loop system so that simulation of PR is possible. In the study by Tang, et. al [17], evaluation of the local stress/strain distributions was more of a curious side note to the measurement of RV function; in this thesis, the main focus is on the evaluation of fiber strains post-PVR as a preliminary step towards identifying possible reverse remodeling mechanisms in various RVEDVIs.

Similar to the goals of this thesis, computational models have previously been used to identify cell-scale mechanisms responsible for organ-level phenomena in electromechanical models of the heart [18]. For example, studies had shown that ventricular dilatation was associated with increased arrhythmogenesis, but the underlying mechanisms were poorly understood. In a study by Li, et. al (2008), computational models in dilated rabbit LVs were developed to test the hypothesis that stretch-activated channel recruitment and geometric deformations in acutely dilated LVs increased arrhythmogenesis [19]. The study found that heterogeneous fiber strain in the ventricular walls resulted in the heterogeneous stretch-activated channel activation and thereby increased the risk of arrhythmogenesis. In a similar manner, this study aims to gain a better understanding of the mechanisms underlying the differences in reverse remodeling after PVR in repaired ToF patients with various RVEDVIs by evaluating post-PVR diastolic fiber strains in a biventricular model of repaired ToF.

In the Cardiac Mechanics Group at UCSD, computational models developed by Krishnamurthy et al. [20] and Kerckhoffs et al. [21] have been able to simulate heart failure and volume- and pressure-overloading of the LV, respectively. In both models, biventricular closed-loop simulations were run over the time scale of several heart beats in order to reach steady state hemodynamics. The models used in this thesis were created by following the methods of Krishnamurthy and Kerckhoffs.

By using a finite-element mesh, these computational models transform the continuous domain that is the patient-specific cardiac geometry into a discretized mesh of nodes and elements that allows complex systems of partial differential equations (that model dynamic tissue properties) to be solved computationally. Each model bridges multiple scales, from subcellular to organ-level mechanics, by the integration of the biventricular geometry, passive mechanical material properties, myofilament active

contractile properties, and hemodynamic pressure boundary conditions in a closed-loop system. Therefore, as technological advancements in computing progress, the impact of computational models in the field of cardiac research should become more apparent by providing greater opportunities to elucidate subcellular mechanisms from organ-level cardiac function.

1.8 Specific Aims

As previously mentioned, eccentric hypertrophy and ventricular dilatation occurs in response to volume overload. Prior studies of the rat LV have shown that eccentric hypertrophy occurs in volume overloaded hearts as a mechanism to normalize diastolic fiber strains, thus adding sarcomeres in series [10], and reversal of the hypertrophy after alleviation of volume-overloading results in the reduced number of sarcomeres in series [11]. Additionally, the distinct shape modes of the RV in repaired ToF patients suggests that regional mechanics may play a significant role in RV remodeling of these patients [15, 16]. In order to alleviate volume overload in repaired ToF patients with an incompetent valve, PVR must be performed, though the timing of the operation remains controversial. While one proposed clinical indicator for PVR is an RV end-diastolic volume index (RVEDVI) greater than 150 mL/m^2, a few studies have found that normalization of RV volume is likely to occur at values higher or lower threshold value than 150 mL/m^2 [22, 14]. However, each study is in agreement that the degree of RV normalization is RVEDVI-dependent, and the underlying mechanism of RVEDVI-dependence is still unclear.

In this thesis, image-based computational models were developed to test the hypothesis that RVEDVI correlates with RV regional diastolic fiber strain immediately after PVR. Two patient-based computational models (one with an RVEDVI of 170 mL/m^2

and one with an RVEDVI of 115 mL/m^2) were developed, and each model underwent full-beat simulations pre-PVR and post-PVR (resulting in a total of four simulations). To test the hypothesis, post-PVR end-diastolic fiber strains in the two models were evaluated and compared because reduction of diastolic fiber strain after PVR may likely affect reverse remodeling in a positive way. Therefore, if lower values of post-PVR diastolic fiber strains were found in the model with RVEDVI of 170 mL/m^2 when compared to that of the model with 115 mL/m^2, then preliminary findings may suggest that more favorable reverse remodeling occurs in patients with higher RVEDVIs.

Chapter 2: Methods

In order to evaluate diastolic fiber strains of the two computational models and test the hypothesis, the computational models first had to be built. This chapter presents the methods by which this was done. The process begins with collection of patient data and continues on to the integration of a passive material model, an active contractile model, and a lumped-parameter circulation model.

Though the majority of past computational cardiac mechanics models focused on LV mechanics and included only the LV in the mesh geometry (with the RV as a lumped parameter), the simplification of a computational model to only the RV in this case is not sufficient in addressing the hypothesis presented in this thesis. Biventricular interactions between each of the model's components are necessary to understand how virtual PVR affects steady-state hemodynamics and mechanics in the RV. For example, PVR is expected to immediately decrease RV preload, but how exactly would steady-state hemodynamic changes be reflected in the RV if the contraction of the LV is not taken into account? Thus, the computational models appropriate for this thesis were biventricular closed-loop functional models, built by following the methods outlined in this chapter. The result of this modeling process was two computational models through which post-PVR regional diastolic fiber strains could be calculated.

2.1 Retrieval of Patient Data

Patient-specific computational cardiac models utilize patient-specific clinical data (i.e., magnetic resonance images, geometric measurements, and catheterization pressures). For this study, de-identified retrospective clinical data of a patient with repaired ToF was acquired from Rady's Children Hospital San Diego. The patient was an asymptomatic 11 year-old male who had a surgical PVR due to severe pulmonary

regurgitation and right ventricular dilatation. RV systolic function was preserved. The patient was evaluated once prior to pulmonary valve replacement and three times post-operation. Table 2.1, below, provides a summary of patient data collected seven months prior to his PVR.

Table 2.1: Summary of Patient Data Seven Months Pre-PVR (*Data estimated from another repaired ToF patient)

Sex	Male
Age (yrs)	11
LVEDV (mL) / LVEDVI (mL/m^2)	109 / 60.2
LVESV (mL) / LVESVI (mL/m^2)	37.7 / 20.8
LV Cardiac Output (L/min)	7.3
LVESP / LVEDP (mmHg)	108* / 15*
RVEDV (mL) / RVEDVI (mL/m^2)	316.6 / 174.9
RVESV (mL) / RVESVI (mL/m^2)	130.6 / 72.1
RV Cardiac Output (L/min)	19
RVESP / RVEDP (mmHg)	32* / 10*
Aorta Diameter (cm)	2.4
Pulmonary Artery Diameter (cm)	2.3
PR fraction	58%

2.2 Biventricular Model Development

The patient-specific biomechanics model was developed by following a protocol that was previously established by UCSD's Cardiac Mechanics Group to model failing hearts [18]. The model consists of four components: a biventricular anatomic model, a passive constitutive model, an active contractile model, and a hemodynamic model. The workflow of building a functional biomechanics model is summarized in Figure 2.1, below.

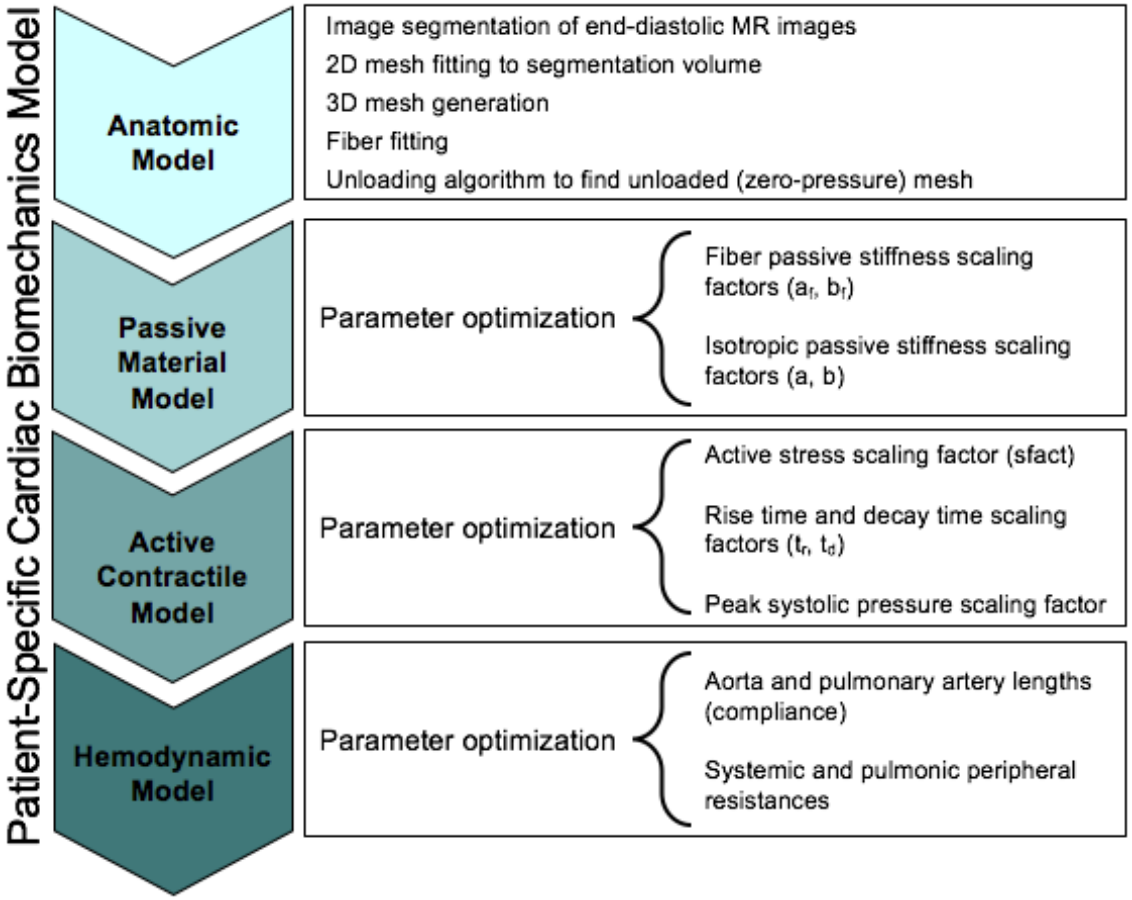

Figure 2.1: Workflow for developing a patient-specific cardiac biomechanics model

2.2.1 Biventricular Anatomic Model

The process of developing the anatomic model is divided into five steps: image segmentation, two-dimensional (2D) mesh fitting, three-dimensional (3D) mesh generation, fiber fitting, and determination of the unloaded geometry. Through this workflow, smooth 3D meshes in the shape of patient-specific ventricular geometries can be extracted from low-resolution MR images. Not only does the resulting discretized mesh better represent the smooth curvature of the real ventricular geometry, but it also allows for the opportunity to solve for systems of partial differential equations that model

dynamic ventricular mechanics. Finally, unloading of the 3D mesh to a zero-pressure state allows for accurate calculation of stresses and strains with respect to an appropriate reference state. The four steps of anatomic model development will be further explained below.

2.2.1.1 Image Segmentation

The patient had a standard 1.5 T cardiac magnetic resonance (MR) exam prior to surgical PVR. Short-axis cine images were acquired with an in-plane resolution of 1.7578 mm x 1.7578 mm (256 x 256 voxels) and a slice thickness of 9 mm. Using the measured heart rate of the patient, 30 images at each slice location were acquired over a single heartbeat. For the purposes of building the 3D biventricular anatomic model, only the short-axis end-diastolic images were used. Manual segmentation of these images was performed using Seg3D, an open-source volume segmentation and processing tool developed by the NIH Center for Integrative Biomedical Computing [23]. Figure 2.2 summarizes the workflow of image segmentation. Images were initially processed using a threshold filter to exclude pixels with intensities greater than that of the myocardium. The epicardial surfaces were manually traced on each image slice using a polyline tool and filled. A Boolean AND operator was then used to filter out the extracardial tissue. Fine adjustments, including removal of trabeculae, were then made using a paintbrush tool. After the myocardial tissue was isolated on each slice, an isosurface was generated.

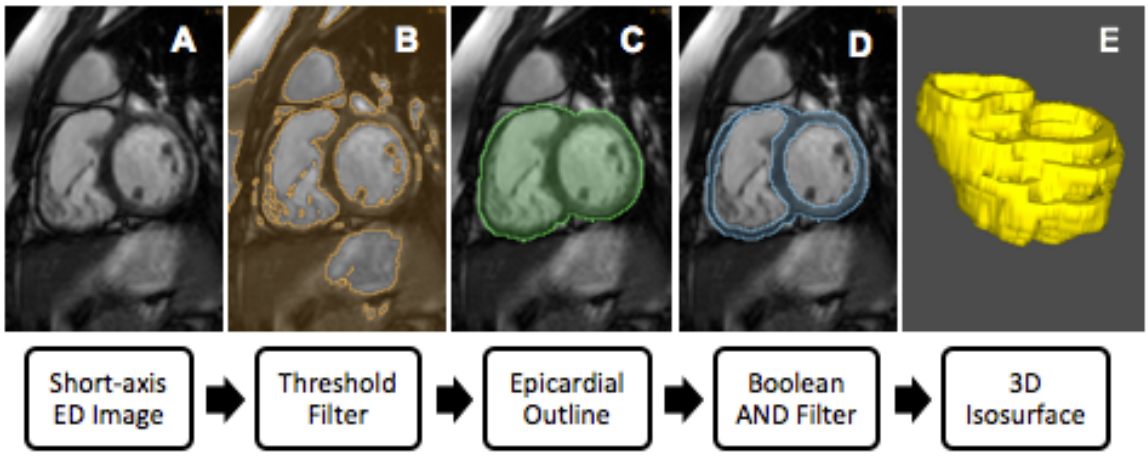

Figure 2.2: Image segmentation workflow showing (A) a raw MR image of a short-axis slice at end-diastole, (B) removal of low-intensity voxels using a threshold filter, (c) manual tracing of the epicardium, (D) application of the Boolean AND operator to masks from (B) and (C), and (E) generation of a 3D isosurface from multiple short-axis slices.

2.2.1.2 Fitting of Two-Dimensional Mesh to Segmentation Volume

The final segmentation volume was exported as STL files to Blender, an open-source 3D graphics and animation software. A template mesh consisting of three 2D surfaces (LV endocardial, RV endocardial, and epicardial) and 109 nodes was fitted manually to the segmentation volume. Node groups were strategically placed near ventricular landmarks and at points of maximal curvature.

2.2.1.3 Three-Dimensional Mesh Generation

The nodal locations of the mesh were imported into Continuity, a problem-solving environment developed at UCSD for multi-scale modeling in bioengineering. The nodes were connected to create 3D elements, transforming the 2D surfaces into a single 3D tri-linear mesh. The scaled Jacobians at each gauss point of the resulting mesh were calculated to check mesh quality (i.e., the face normals of each element do not cross extensively). If the scaled Jacobian demonstrated poor mesh quality at certain element

locations, nodal positions were readjusted in Blender. The mesh was then refined once transmurally and nodal derivatives were computed with respect to arc lengths, resulting in a smoothed 3D tri-cubic hermite mesh with 209 nodes and 128 elements, as shown in Figure 2.3, below.

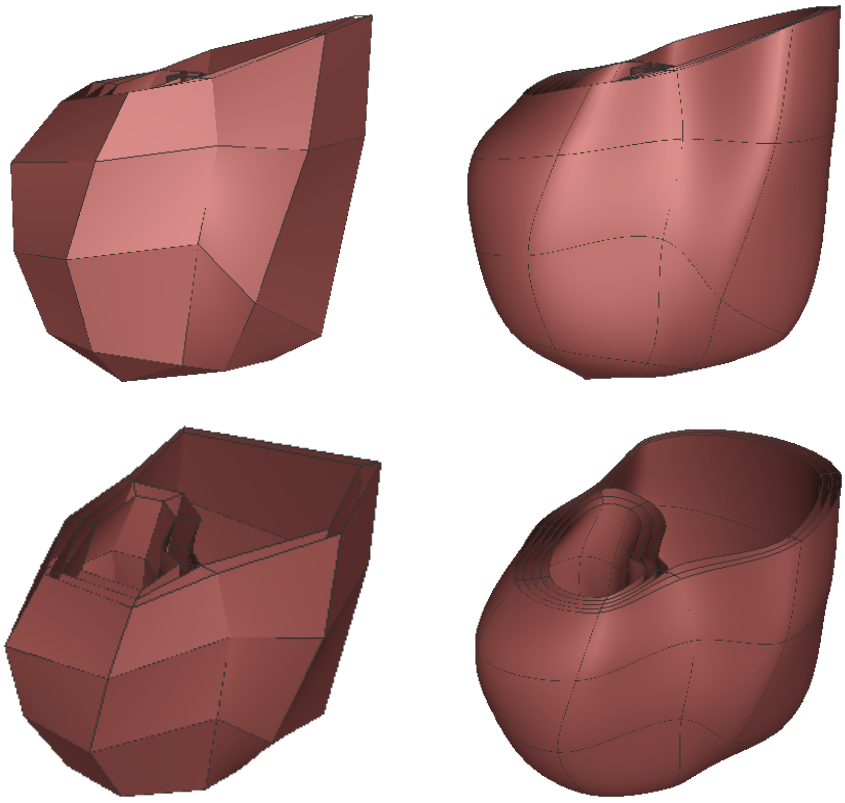

Figure 2.3: 3D mesh prior to (left) and after (right) transmural refinement and smoothing.

2.2.1.4 Fiber Fitting

Fiber vectors were assigned at each node according to a template derived from diffusion-tensor MRI of an isolated, fixed human organ donor heart [20]. Transformation of the fiber architecture from the donor heart anatomy to the anatomy of the patient was achieved using large deformation diffeomorphic mapping.

2.2.1.5 Unloading Algorithm

The main goal of the unloading algorithm is to iteratively find an unloaded (zero-pressure) mesh that, when passively inflated to the measured end-diastolic pressure, is able to reproduce the end-diastolic MR-derived 3D mesh. The algorithm began with an an initial guess of the unloaded geometry, which in this case, was the MR-derived mesh itself. The mesh was passively inflated to the measured end-diastolic ventricular pressures (*Note: see next section regarding passive material properties). Though the patient did not have clinically measured pressures at end-systole and end-diastole, pressure values were estimated using measurements from another repaired ToF patient with similar body surface area, as stated previously in Table 2.1.

After inflation, the difference between the inflated mesh and the desired MR-derived mesh was calculated using the deformation gradient. The inverse of the deformation gradient was then applied to the initial guess for the unloaded geometry. The new guess for the unloaded geometry was again inflated to the measured end-diastolic pressures, and the deformation gradient was calculated. This process was performed iteratively until the inflated mesh closely matched the MR-derived mesh. Acceptance criteria was determined to be a root-mean-square error (RMSE) of corresponding nodal positions less than 1.75758 mm, the resolution of the MR data.

In order to validate that the correct unloaded geometry and LV end-diastolic pressure-volume relation (EDPVR) were reached, the unloaded mesh volume and simulated LVEDPVR were compared to the Klotz empirical unloaded volume and Klotz empirical LVEDPVR, respectively [24]. Klotz et al. proposed a few empirical equations for the determination of the LV unloaded volume (Equation 2) and LVEDPVR (Equations 3-5) using measured diastolic volume and pressure measurements [24]. In the equations

below, P_m and V_m correspond to left ventricular pressure and volume measured during diastole, respectively.

$$\mathbf{V_0 = (0.6 - 0.006P_m)V_m} \quad (2)$$

In order to account for most differences in patient population, even in failing hearts and across various species, the Klotz LVEDPVR is normalized, as shown below.

$$\mathbf{V_{30} = V_0 + \frac{(V_m - V_o)}{\left(\frac{P_m}{A_n}\right)^{\frac{1}{B_n}}}} \quad (3)$$

$$\mathbf{EDV_n = \frac{EDV - V_0}{V_{30} - V_0}} \quad (4)$$

$$\mathbf{EDP = A_n (EDV_n)^{B_n}} \quad (5)$$

A_n and B_n are parameters with the values of 28.2 mmHg and 2.79, respectively.

2.2.2 Passive Material Model

The passive material properties were modeled by the slightly compressible form of the orthotropic constitutive model developed by Holzapfel and Ogden [25]. The strain-energy equation has four terms, with the first term representing isotropic passive properties, the second term representing transversely isotropic properties, the third term representing orthotropic properties, and the fourth term representing the slight compressibility of the myocardium [26], as shown in Equation 1 below.

$$\boldsymbol{\psi} = \frac{\mathbf{a}}{\mathbf{2b}} \mathbf{e}^{\left(\mathbf{b}(\mathbf{I_1}-\mathbf{3})\right)} + \sum_{i=f,s} \frac{\mathbf{a_i}}{\mathbf{2b_i}} \left(\mathbf{e}^{\left(\mathbf{b_i}(\mathbf{I_{4i}}-\mathbf{1})^{\mathbf{2}}\right)} - 1\right) + \cdots$$
$$\frac{\mathbf{a_{fs}}}{\mathbf{2b_{fs}}} \left(\mathbf{e}^{\left(\mathbf{b_{fs}}\mathbf{I_{8fs}}^{\mathbf{2}}\right)} - 1\right) + \frac{\kappa}{2} (\det(F) - 1) \ln(\det(F)) \quad (1)$$

I_1 corresponds to the first invariant of the right Cauchy-Green strain tensor, I_{4i} corresponds to the components of the right Cauchy-Green strain tensor in the fiber and sheet directions, I_{8fs} corresponds to the component of the right Cauchy-Green tensor in the fiber-sheet direction, and F corresponds to the deformation gradient. The parameters

a, b, a_f, b_f, a_s, b_s, a_{fs}, and b_{fs} are positive material constants, and κ is the bulk modulus. All a parameters have dimensions of stress, and b parameters are dimensionless.

During the unloading algorithm, parameter values were initially set to the average values determined by Krishnamurthy et al. [20] for the patient-specific modeling of heart failure. Three other sets of parameter values were also used, changing the pressure scaling parameters a and a_f and the exponential scaling parameters b and b_f. After iterations of passive inflation and deflation, the final deflated mesh volumes of each test case were compared to the Klotz unloaded volume, the simulated LVEDPVRs were compared to the Klotz LVEDPVR, and the inflated meshes were compared to the MR-derived mesh using the RMSE.

2.2.3 Active Contractile Model

The active contractile properties of the heart were modeled by a three-wall segment Hill-type model developed by Lumens et al. called the TriSeg model [27]. The model assumes that the heart is divided into three distinct walls: the left ventricular free wall, interventricular septal wall, and right ventricular free wall. By describing global organ-level mechanics through cell-scale myofiber mechanics, conservation of energy was satisfied.

2.2.4 Hemodynamic Model

The hemodynamics were modeled by a closed-loop lumped-parameter model developed by Arts et al. called CircAdapt [28]. CircAdapt simulates beat-to-beat dynamics of the four-chamber heart, dividing the main components of the circulatory system into four modules: chambers, tubes, valves, and resistances. The physiological relevance of the model parameters makes this model particularly useful in reflecting

changes to the circulation due to pulmonary regurgitation. Specifically, valves are defined by three parameters: orifice length, lumen area when open, and lumen area when closed. The patient's severe pulmonary regurgitation was implemented by changing the pulmonary valve lumen area when closed to match the valve lumen area when open.

2.2.5 Closed-Loop Biomechanical Model

After determining the correct unloaded geometry and passive material properties of the patient, full-beat mechanics were simulated by incorporating the unloaded mesh, the passive material model, active contractile model and hemodynamic model in a closed-loop system. Full-beat simulations were run for several beat cycles until steady-state was reached. Initial parameter values for the CircAdapt model and active contractile model were taken from the average biventricular model developed by Krishnamurthy et al. [20], though heart rate and cardiac output values were adjusted to reflect measurements from the patient. Active material parameters and hemodynamic parameters were optimized in order to reach the appropriate end-systolic pressure and volume. After the model was matched with the desired pressures and volumes from patient measurements, virtual PVR was simulated by changing the pulmonary valve lumen area when closed to approximately zero.

2.2.6 Simulation of Various RVEDVIs

In the first model (Model #1), the anatomy was patient-derived, exhibiting an RVEDVI of 170 mL/m^2 similar to that measured clinically. Following the completion of building the first model, a second model (Model #2) was created by adjusting Model #1's mesh in Blender to decrease the RVEDVI to approximately 115 mL/m^2 while keeping all

other dimensions the same. Nodes of the RV free wall were moved manually towards the center of the RV cavity. The mesh went through the unloading algorithm, using the same ventricular pressures and passive material properties as Model #1. After the unloaded geometry was found, full beat simulations were run using the same active material properties and hemodynamic parameters as Model #1. Therefore, a total of four full beat simulations were completed—two RVEDVIs, each before and after virtual PVR.

Pressure-volume loops were drawn for each simulation to observe whether the virtual PVR in both Models #1 and #2 were able to reproduce the clinically expected changes in steady-state ventricular function (i.e., decreased RVEDV, increased LVEDV, and increased LV cardiac output). In order to directly address the hypothesis of this thesis, post-PVR end-diastolic fiber strains in the RV free wall were evaluated and recorded in each model.

Chapter 3: Results

3.1 Image Segmentation and Mesh Fitting

In the short-axis MR series of the patient, the LV myocardium appeared in nine of the fourteen slices, compared to the RV myocardium that appeared in twelve slices. This offset can be accounted for by the large RV size and the demonstrated basal bulging that is typical of RV shape in repaired ToF [15]. To include as much of the RV ventricular volume as possible, the basal plane used for 2D surface fitting was tilted. Figure 3.1 shows the refined 3D mesh overlaid onto the raw data of the patient, as represented by the black dots. The mesh ventricular volumes were calculated in Continuity, resulting in an LVEDV of 113 mL and RVEDV of 314 mL (compared to clinically reported values of 109 mL and 316.6 mL, respectively).

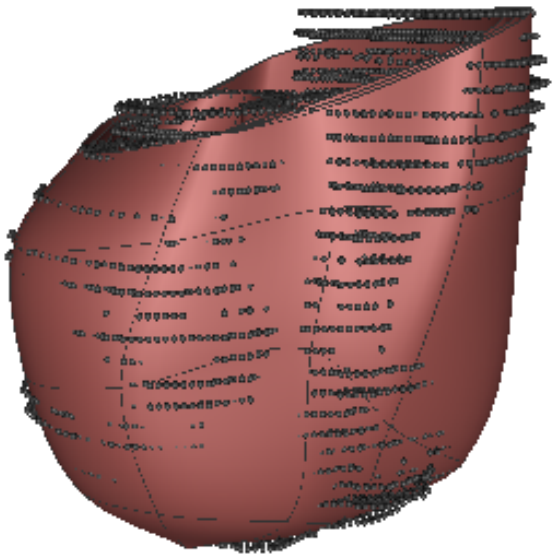

Figure 3.1: Refined finite-element mesh of Model #1 fitted to the end-diastolic MR data of the patient, shown as black dots.

3.2 Unloading Algorithm

Initially, the values used for the passive material parameters (a, a_f, b, b_f) were the average values used by Krishnamurthy et al. in patient-specific models of heart failure.

In addition, various sets of parameter values were run simultaneously to determine what values most accurately reflected the Klotz EDPVR and unloaded volume. Using the measured LV end-diastolic pressure of 15 mmHg and the MR-derived mesh LV volume of 113 mL in the Klotz empirical equations, the unloaded LV volume was determined to be 58 mL. During the unloading algorithm, iterations of inflation and deflation were performed until an unloaded mesh produced an unloaded LV volume and LVEDV within 5% of the expected values. The LV EDPVR curves generated at each inflation step are shown in Figure 3.2. Because the initial guess for the unloaded geometry was the MR-derived mesh, the preliminary inflation curve was omitted to view changes in subsequent iterations more clearly. By the fourth iteration, the unloaded geometry produced an unloaded LV volume of 60 mL (+3.4%) and LVEDV of 111 mL (-1.8%).

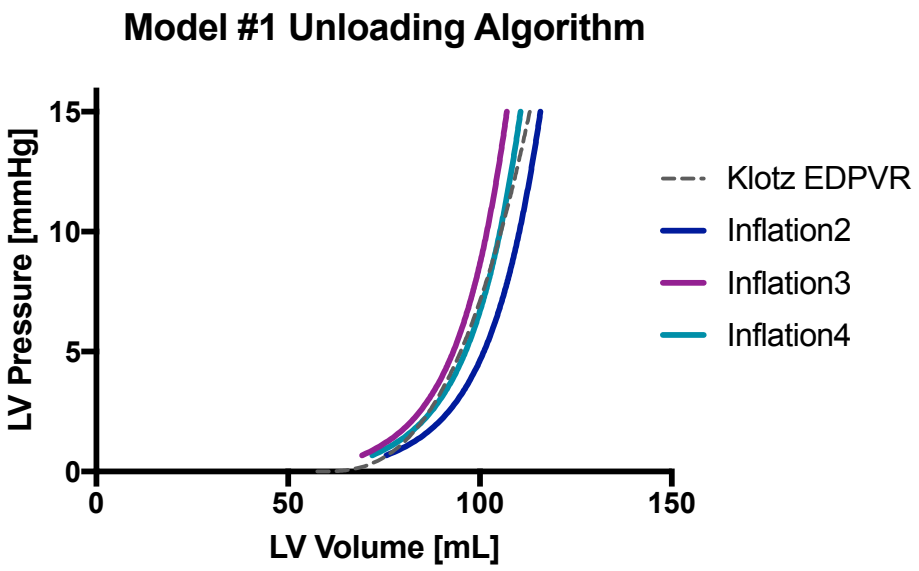

Figure 3.2: LVEDPVR graphs showing Klotz' empirical curve and simulation results for each iteration (after initial inflation) of the unloading algorithm for Model #1.

Additionally, the maximum RMS error of the nodal positions of the inflated mesh and MR-derived mesh was required to be less than 1.7578 mm, the in-plane resolution

of the MR images. Figure 3.3 shows that the maximum RMS error of the nodal positions is well below the in-plane resolution by the third inflation.

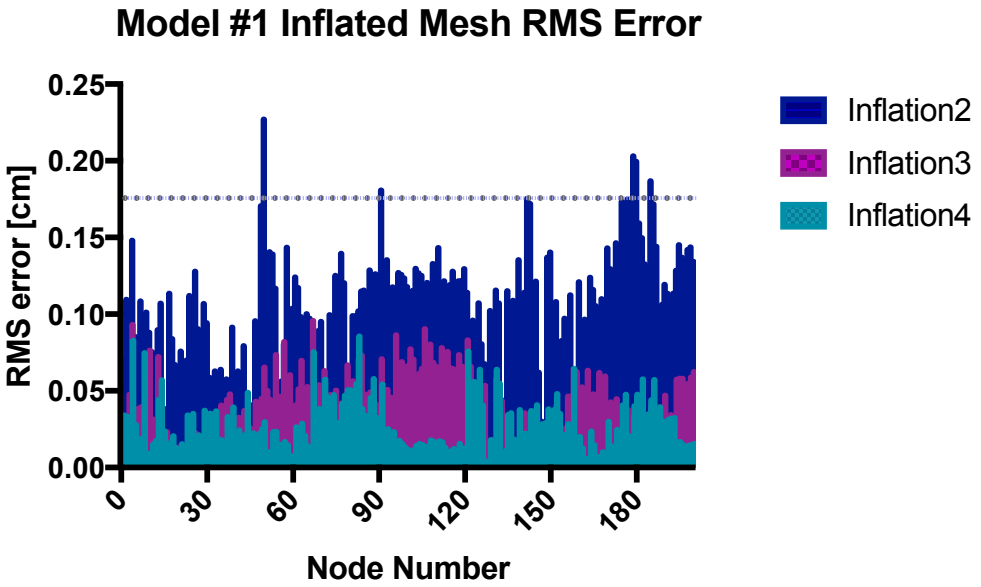

Figure 3.3: Root-mean-square error of the inflated mesh versus the MR-derived mesh nodal positions after each iteration of passive inflation for Model #1.

Therefore, in order to satisfy each acceptance criteria, the unloaded geometry resulting in Inflation 4 was selected as the correct unloaded geometry. Figure 3.4 shows the final unloaded geometry, left, and inflated geometry, right.

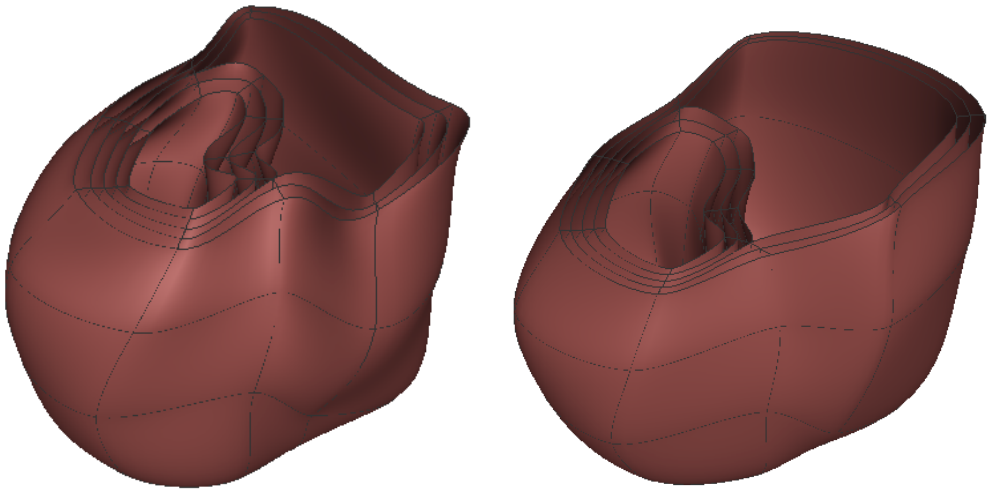

Figure 3.4: Final unloaded mesh (left) and inflated mesh (right) of Model #1 after unloading algorithm.

3.3 Closed-loop Full Beat Simulations

The pulmonary regurgitant fraction was calculated by dividing the volume of blood entering the RV during isovolumic relaxation by the volume of blood ejected by the RV during systole. In Model #1, RV isovolumic relaxation was impaired. The pulmonary regurgitant fraction was calculated to be 50%, as half the amount of blood ejected during systole returned to the RV during the isovolumetric relaxation period (Figure 3.5).

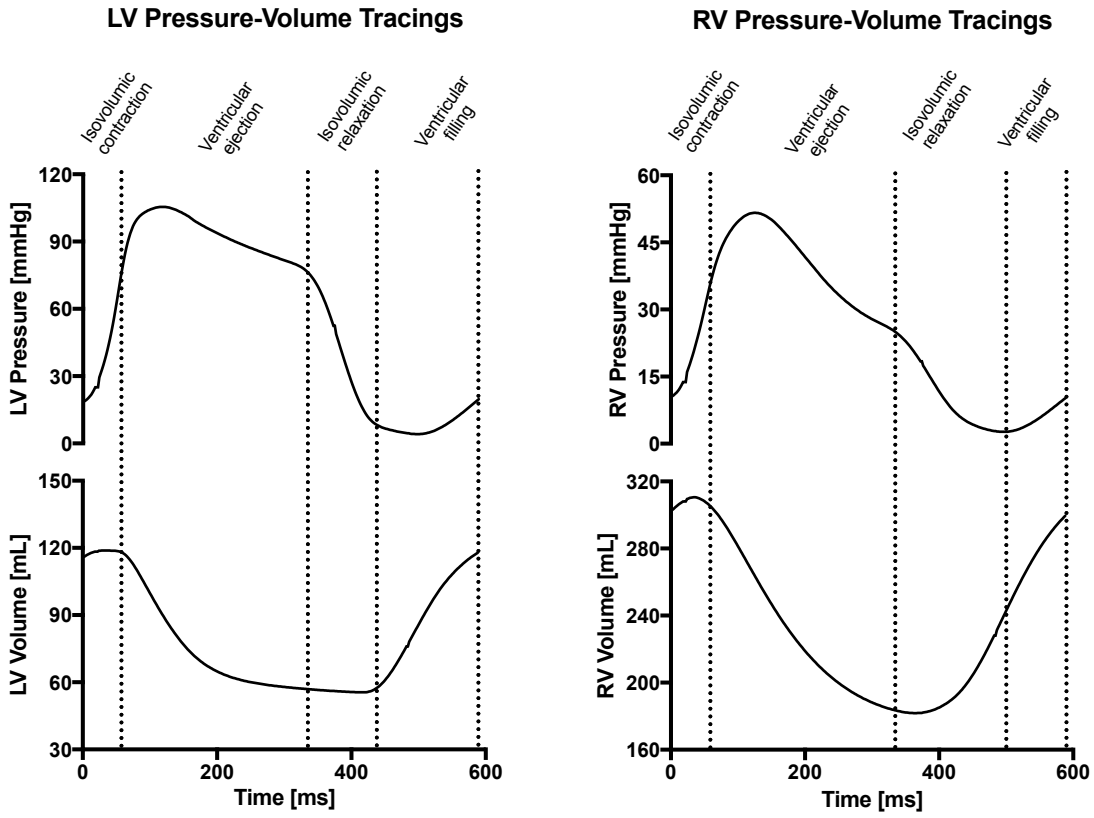

Figure 3.5: Pressure and volume tracings of Model #1 over a single steady-state beat prior to PVR.

Figure 3.6 shows the pressure-volume (P-V) loops for both the LV and RV before and after PVR. The purple dotted line, representing the RV P-V loop prior to PVR, demonstrates non-isovolumic contraction and relaxation. The significant preload in the RV due to regurgitant flow results in a stroke volume of approximately 125 mL and a

cardiac output of approximately 12.8 mL/min. The solid purple line, representing the LV P-V loop prior to PVR has a stroke volume of approximately 62 mL and a cardiac output of approximately 6.3 mL/min. After simulation of PVR by reduction of the closed pulmonary valve lumen area to approximately zero, a new steady-state state was reached. The RV demonstrated an improved isovolumic contraction and relaxation and a reduced stroke volume (~75 mL), as shown by the dotted teal line. Though RV cardiac output was reduced to 7.6 mL/min, the LV still experienced an increase in preload. Because reversal of flow across the pulmonary valve was eliminated, the net volume of blood delivered to the LV per cycle increased. The LV stroke volume and cardiac output therefore increased to 69 mL and 7 mL/min, respectively.

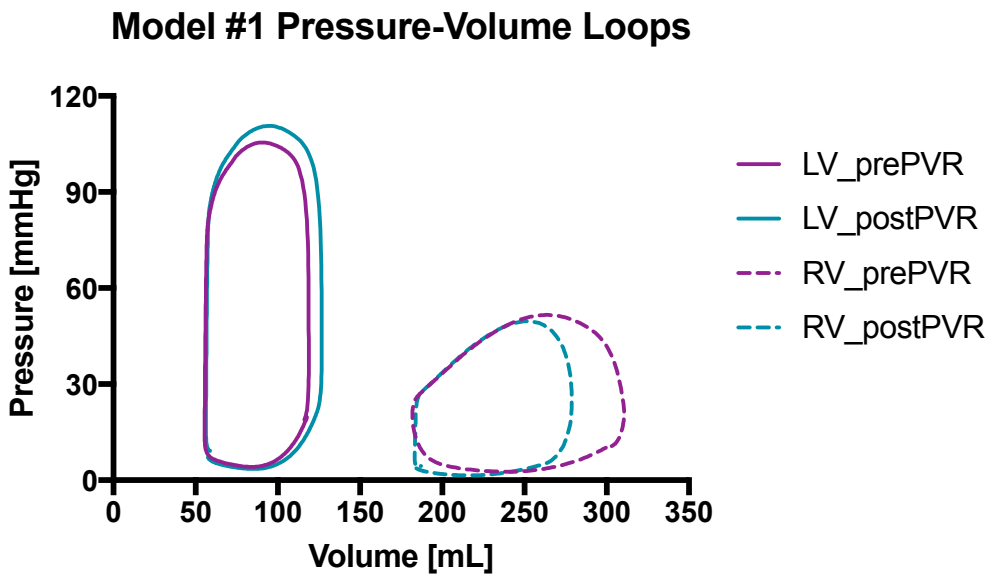

Figure 3.6: Pressure-volume loops for Model #1 showing the effect of PR reduction by PVR (prePVR = model with 50% pulmonary regurgitant fraction, postPVR = model with 0% pulmonary regurgitant fraction).

End-diastolic Lagrangian fiber strains, E_{ff}, were calculated at the twenty-seven integration points of each element in the RV free wall (RVFW). The RVFW has a height

of 3 elements (from apex to base), a length of 4 elements, and a width (transmurally) of 2 elements. Negative values of E_{ff} were found in 7 of the 24 RVFW elements, most likely due to solutions that did not converge very well converged on the low resolution finite-element mesh. The mean E_{ff} of the RVFW elements (excluding the elements exhibiting negative values) were found to be 0.056 and decreased to 0.047 after virtual PVR (16% decrease). The pre-PVR and post-PVR mean E_{ff} were then averaged again transmurally, and each region was plotted in Figure 3.7. In each polar plot, the inner ring represents the RVFW regions near the apex and the outer ring represents the RVFW regions near the base. At the very top of each plot are the most anterior RVFW regions, and at the very bottom are the most posterior RVFW regions.

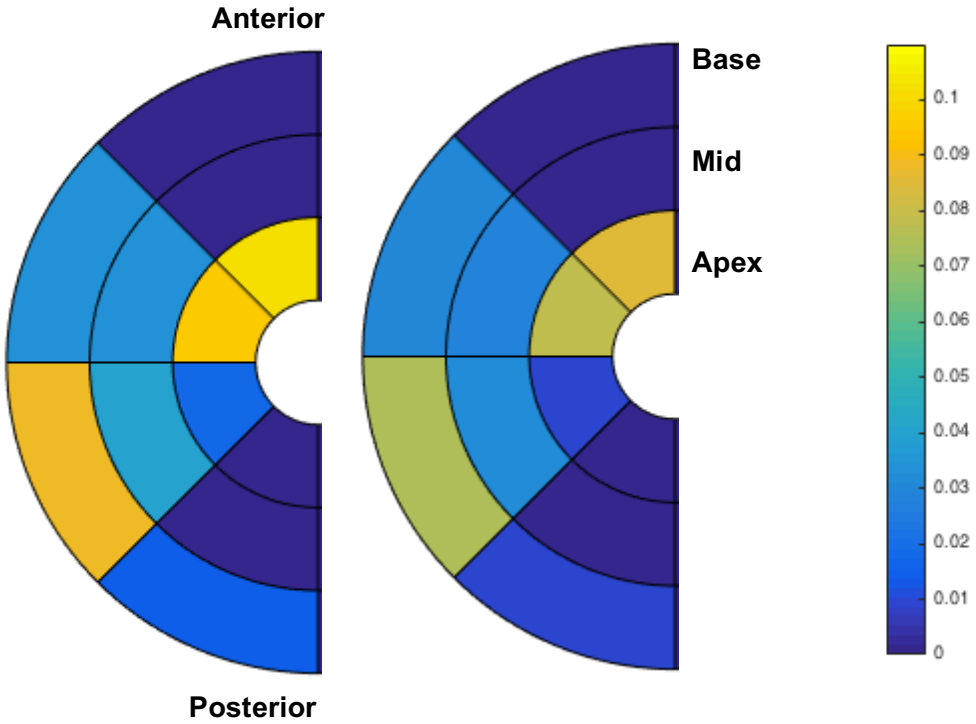

Figure 3.7: Polar plots of mean E_{ff} for each RVFW region in Model #1, pre-PVR (left) and post-PVR (right).

As shown in each of the positive-valued elements in Figure 3.7, the mean E_{ff} within each region decreased after PVR, which should be expected.

3.4 Simulations Using Patient Mesh with Reduced RVEDVI

The RVFW nodes of the Model #1's mesh were then altered to produce a mesh with a lower RVEDVI of 115 mL/m^2 for Model #2. The resulting mesh was unloaded using the same ventricular ED pressures. The unloaded and inflated meshes, pressure and volume tracings, and steady-state P-V loops are shown in Figures 3.9, 3.10, and 3.11, respectively. The difference in RV geometry of the unloaded and inflated meshes with respect to Model #1 is apparent when comparing the images found in Figures 3.4 and 3.18.

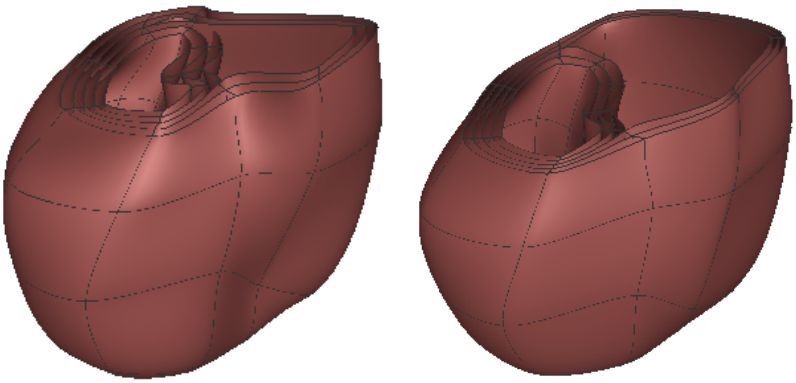

Figure 3.8: Final unloaded mesh (left) and inflated mesh (right) of Model #2 after unloading algorithm.

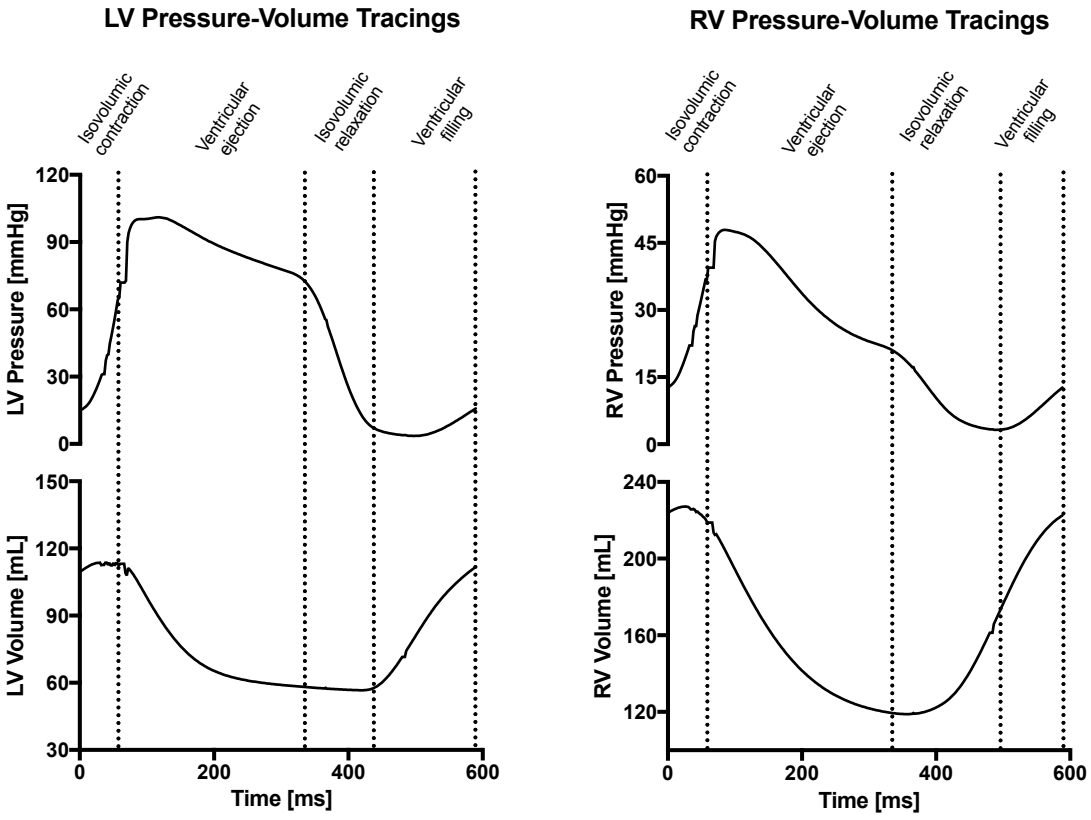

Figure 3.9: Pressure and volume tracings of Model #2 over a single steady-state beat prior to PVR.

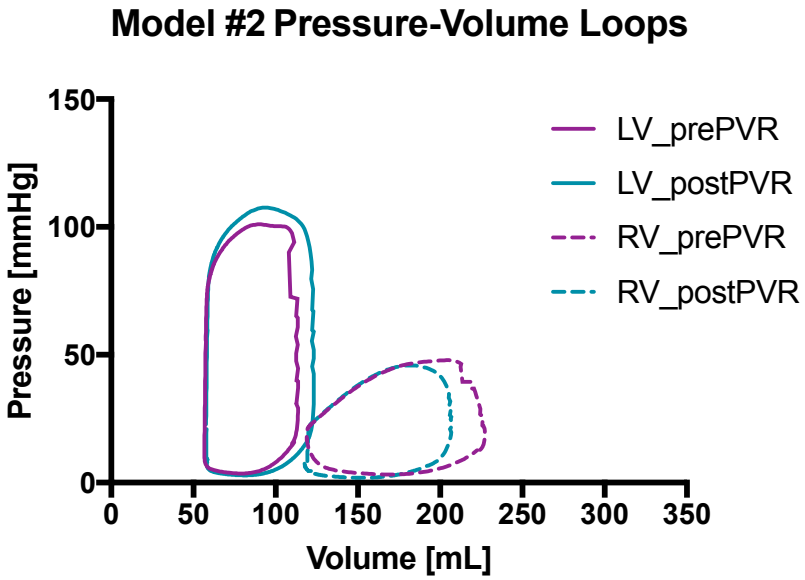

Figure 3.10: Pressure-volume loops for Model #2 showing the effect of PR reduction by PVR.

Table 3.1: Summary Table of Steady-State Cardiac Measurements

	Patient	**Model #1**		**Model #2**	
	Pre-PVR	*Pre-PVR*	*Post-PVR*	*Pre-PVR*	*Post-PVR*
LVEDV (mL)	109	120	126	111	120
LVESV (mL)	37.7	58	58	61	61
LV CO (L/min)	7.3	6.3	6.9	5.1	6.0
LVESP / LVEDP (mmHg)	108* / 15*	86/ 22	86 / 25	82 / 15	82 / 17
RVEDV (mL)	316.6	306	263	223	204
RVESV (mL)	130.6	181	182	118	118
RV CO (L/min)	19	12.8	8.2	10.7	8.8
RVESP / RVEDP (mmHg)	32* / 10*	25 / 12	25 / 6	17 / 13	17 / 6
PR fraction	58%	50%	0%	58%	0%
Mean (+) RVFW E_{ff}	-	0.056	0.047	0.063	0.060

As done previously with Model #1, the stroke volume, cardiac output, and pulmonary regurgitant fraction of Model #2 at steady-state were calculated. Table 3.1, above, summarizes the measured values from the patient and both models. Full-beat simulations of both models were able to produce expected changes in steady-state cardiac measurements in response to virtual PVR (i.e., decrease in RV EDV, decrease in RV cardiac output, increase in LV preload, and observation of isovolumic contraction and relaxation). However, measurements in the mesh of Model #1 did not accurately match clinically measured values from the patient prior to PVR, with the most significant differences being the ventricular ESVs. Additionally, cardiac output of both the RV and LV should theoretically be equal after simulation of PVR. However, in both models, this was not the case, suggesting that steady-state has not yet been reached.

Similar to Model #1, after full-beat simulations of Model #2 were completed, mean values of positive E_{ff} values in RVFW elements was calculated. The mean E_{ff} values pre-PVR and post-PVR were 0.063 and 0.060, respectively. Figure 3.11 shows the mean E_{ff} of RVFW regions pre-PVR and post-PVR in Model #2.

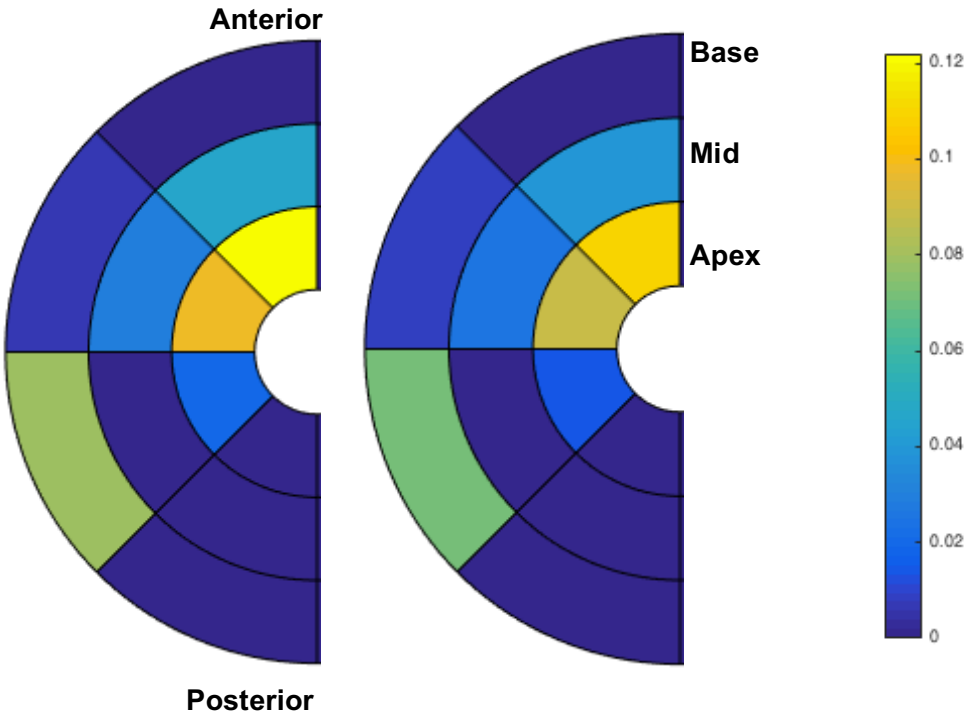

Figure 3.11: Polar plots of mean E_{ff} for each RVFW region in Model #2, pre-PVR (left) and post-PVR (right).

Like Model #1, the general trend of mean regional E_{ff} is a decrease after PVR. However, in Figure 3.11, a slight increase is seen in the basal posterior region farthest from the septal wall, and in the mid anterior region closest to the septal wall. Model #2's mesh also has one more negative region than Model #1, suggesting that the accuracy of the solutions may be questionable in a larger portion of Model #2.

To address the hypothesis that RVEDVI correlates with regional diastolic E_{ff}, the post-PVR diastolic E_{ff} between the corresponding regions in the two models were then compared. Though various regions exhibited negative values of E_{ff}, those regions were still used for relative comparisons between the two models. Therefore, the comparison

was made by calculating the difference in the post-PVR magnitudes of the regional diastolic fiber E_{ff} between Models #1 and #2 and plotting them in Figure 3.12.

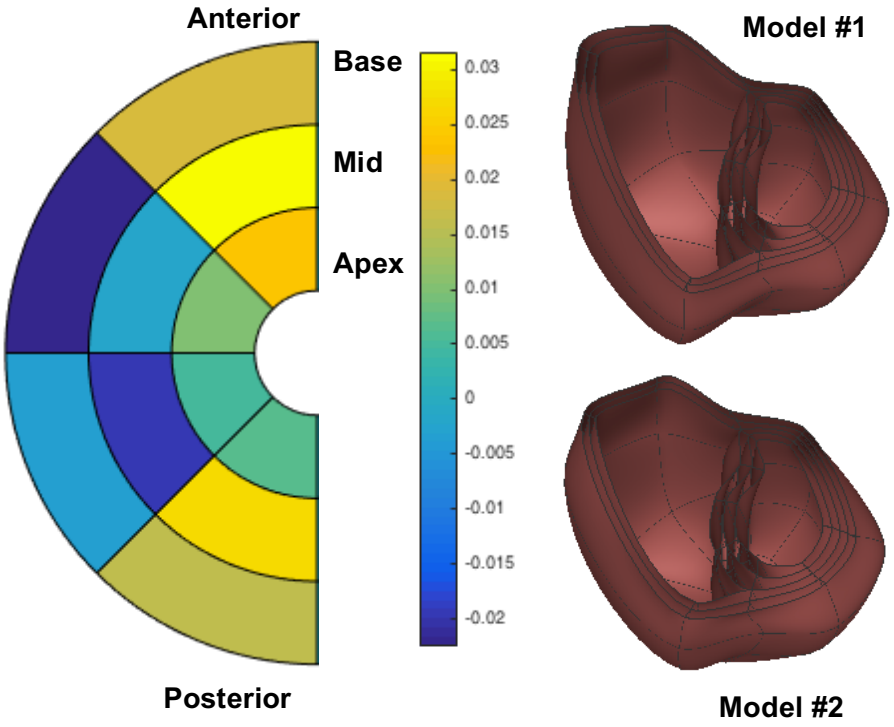

Figure 3.12: Polar plot of differences in post-PVR diastolic E_{ff} magnitudes between Models #1 and #2 (positive values represent a higher strain in Model #2 than in Model #3), and images of end-diastolic meshes.

The relative comparison of the post-PVR regional diastolic E_{ff} in Models #1 and #2 suggest that post-PVR fiber strain in Model #2 is greater in RVFW regions closest to the septum, which is also where the greatest differences in curvature exist between the two models.

Chapter 4: Discussion

4.1 Full Beat Simulation Findings

In this thesis, one patient-specific and one patient-based computational model was developed to test the hypotheses that RVEDVI correlates with post-PVR regional diastolic fiber strains. Though this thesis only presents two computational models as a preliminary study of biomechanics in repaired ToF patient, the main findings of this thesis are that: (1) regional RVFW diastolic E_{ff} generally decreases after PVR, and (2) the magnitudes of post-PVR diastolic E_{ff} in RVFW regions near the septal wall were relatively lower in Model #1 than in Model #2.

These preliminary findings suggest that RVEDVI may correlate with a decrease in post-PVR regional diastolic fiber strains, particularly in regions of high curvature, such as the RVFW adjacent to the septal wall. Sheehan et al.'s study of RV remodeling in repaired ToF [15] found that the RV cross-sectional area in repaired ToF patients was rounder than normal patients, as exhibited by bulging of the RVFW. Therefore, regional RV remodeling in the RVFW near the septal wall may be responsible for these directional RV shape changes. The preliminary findings of this thesis may suggest that, like RV forward remodeling, RV reverse remodeling may also be more likely to occur in regions of the RVFW near the septal wall, and that the degree of reverse remodeling may be greater in patients with greater RVEDVIs at the time of PVR.

However, these findings are only clinically relevant after further validation and investigation. Though prior studies have shown that eccentric hypertrophy in a volume overloaded heart correlates with the normalization of diastolic fiber strains, reverse remodeling is still not very well understood. Alleviation of excessive strains after PVR may prevent further RV dilatation, but the mechanisms behind reverse remodeling and normalization of RV size must be further investigated.

4.2 Model Limitations

Though the patient-specific model is able to produce physiologically relevant pressure-volume and stress-strain data, the model has many limitations, beginning with the development of the anatomic model. The MR exam was performed at 1.5 Tesla with a low in-plane resolution of 1.7578 mm x 1.7578 mm and large slice thickness of 9 mm. Due to the thin RV walls, partial volume effects and motion artifacts played a significant role in image segmentation by limiting accuracy of wall thicknesses. The large slice thickness resulted in a segmentation volume with coarse layers. Therefore, when the 2D surfaces were fitted to the volume, data between layers had to be estimated by interpolation.

The 2D mesh surfaces also presented its own significant limitations in representing the patient geometry. When constructed into a 3D mesh, the template contains 128 elements, with a height of three elements on the RV free wall and a height of four elements on the LV free wall. This asymmetry between the two ventricles is useful in reflecting the larger relative volume of the LV in normal hearts. The layout of the template allows for elements to remain fairly cubic at the base and septal wall of normal hearts. In modeling the severely dilated RV in patients with repaired ToF, fidelity to patient geometry is compromised in order to maintain good mesh quality. As a result, the template mesh tends to underestimate the RV endocardial volume and overestimate the LV endocardial volume in patients. Additionally, the RV of the patient demonstrates high curvature of the free wall near the septum due to RV dilatation. With only four elements along the length of the ventricular free wall, the refined mesh was not able to accurately match the RV shape, which may have a significant effect on simulated diastolic strain values of the RVFW.

When matching the model of the patient to measured ventricular pressures, the pressures from another repaired ToF patient were used due to the lack of catheterization data. Though the body surface area and LV values of the other patient were similar to that of the patient being modeled, the ventricular pressures may have differed. An underestimation of the ventricular pressure would cause the unloaded volume to be smaller than the actual unloaded volume, resulting in inaccurate stress-strain calculations. Therefore, the lack of patient-specific data prevents the full validation of the model.

This model only reflects the reduction in PR due to PVR, but does not include other changes due to PVR, such as scarring or reduced compliance in the RVOT. In patients that had complete repair done with a transannular patch, the incision of the RVOT results in scarring. Similarly, surgical PVR requires a repeat ventriculotomy, which would result in a repeat scar within the RVOT. In both cases, the scarred region may become hypokinetic, meaning that the region does not contract very well. In these patients, temporal dyskinesis of the two ventricles may also be present. Because this model assumes homogeneous material properties throughout the ventricles and does not integrate electrophysiology, scarring of the RVOT and temporal dyskineses between the two ventricles is not included in the model.

With respect to the circulatory model, regulation of blood pressure by the fast acting baroreflex response was not included. Therefore, heart rate, contractility, and peripheral resistance—the main properties altered by the baroreflex response—remained constant throughout the simulation.

Due to the sensitivity of the model to material properties and circulatory parameters, various sets of parameters resulted in a diverged solution of the full beat mechanics before reaching steady-state. Therefore, in order to find a converged solution

at approximately steady-state, optimization of model parameters to match clinical measurements was compromised.

4.3 Computational Limitations

Due to the complexity of the patient-specific model, computation time was relatively long. For the unloading algorithm of the models' meshes, three iterations were required to reach the correct unloaded geometry. Each case took approximately 12 hours to run. Initial optimization of the passive material properties and adjustment of the MR-derived mesh resulted in numerous unloading trials in order to obtain a correct unloaded geometry that would successfully converge.

Running the full beat simulations required the most computational effort. The first full beat required an average of 13 hours to complete, with subsequent beats requiring an average of 5 hours. Computation time differed for each trial, depending on how many iterations it took for the solution to converge at each step. Therefore, optimization of the active contractile parameters and circulatory parameters was difficult to perform in a timely manner.

Chapter 5: Concluding Remarks

As a follow up to this preliminary work, an appropriate next step would be to perform the same simulations on a larger number of models, with RVEDVIs incrementing by 10 mL/m^2 from 120 mL/m^2 to 220 mL/m^2, and to evaluate the post-PVR regional diastolic fiber strains at each RVEDVI. The current study was severely limited by the resolution of the finite-element mesh, especially due to the increased curvature of the RVFW adjacent to the septal wall; future works should try to refine the mesh further and re-run simulations, provided that the computation time does not increase greatly. If remodeling and reverse remodeling are in fact more likely to occur in RVFW regions nears the septal wall, altering the RV geometry to produce different RVEDVIs must be performed carefully to match mean RV shapes observed in repaired ToF patients. This thesis focused primarily on the post-PVR regional diastolic fiber strains. However, post-PVR regional diastolic fiber strains in future works may also be interesting to evaluate.

Though this thesis is only a preliminary study, patient-specific modeling of PVR in repaired ToF patients has shown potential to provide insight into cell-scale mechanisms for organ-level mechanics. Results from this thesis were able to produce pressure-volume changes similar to those seen in clinical measurements before and after PVR in patients with repaired ToF— decrease in RV EDV and RV cardiac output, increase in LV preload and LV cardiac output, and observation of isovolumic contraction and relaxation. Additionally, the main findings of this thesis demonstrate that RVEDVI may correlate with post-PVR regional diastolic fiber strains, particularly in the RVFW region adjacent to the septal wall.

REFERENCES

[1] Tracy RE, Sander GE. Histologically measured cardiomyocyte hypertrophy correlates with body height as strongly as with body mass index. Cardiology research and practice. 2011 Jun 8;2011.

[2] Helm P, Beg MF, Miller MI, Winslow RL. Measuring and mapping cardiac fiber and laminar architecture using diffusion tensor MR imaging. Annals of the New York Academy of Sciences. 2005 Jun 1;1047(1):296-307.

[3] Bailliard F, Anderson RH. Tetralogy of fallot. Orphanet journal of rare diseases 4.1 (2009): 1.

[4] Chessa M, Giamberti A. The Right Ventricle in Adults with Tetralogy of Fallot. Springer; 2012 Apr 3.

[5] Gaillard F. Tetralogy of Fallot - Diagram. Radiopaedia Blog RSS. Radiopaedia, Apr. 2016. Web. 16 May 2016.

[6] Ammash NM, Dearani JA, Burkhart HM, Connolly HM. Pulmonary regurgitation after tetralogy of Fallot repair: clinical features, sequelae, and timing of pulmonary valve replacement. Congenital heart disease. 2007 Nov 1;2(6):386-403.

[7] Tetralogy of Fallot Repair. Digital image. Procedure Illustrations. The Children's Heart Clinic, 2014. Web.

[8] Karl TR. Tetralogy of Fallot: current surgical perspective. Annals of pediatric cardiology. 2008 Jul 1;1(2):93.

[9] Powell AJ, Lock JE, Keane JF, Perry SB. Prolongation of RV-PA Conduit Life Span by Percutaneous Stent Implantation Intermediate-Term Results. Circulation. 1995 Dec 1;92(11):3282-8.

[10] Emery JL, Omens JH. Mechanical regulation of myocardial growth during volume-overload hypertrophy in the rat. American Journal of Physiology-Heart and Circulatory Physiology. 1997 Sep 1;273(3):H1198-204.

[11] Gerdes AM. Cardiac myocyte remodeling in hypertrophy and progression to failure. Journal of cardiac failure. 2002 Dec 31;8(6):S264-8.

[12] Armstrong AK, Balzer DT, Cabalka AK, Gray RG, Javois AJ, Moore JW, Rome JJ, Turner DR, Zellers TM, Kreutzer J. One-year follow-up of the Melody transcatheter pulmonary valve multicenter post-approval study. JACC: Cardiovascular Interventions. 2014 Nov 1;7(11):1254-62.

[13] Geva T. Indications for pulmonary valve replacement in repaired tetralogy of Fallot the quest continues. Circulation. 2013 Oct 22;128(17):1855-7.

[14] Frigiola A, Tsang V, Bull C, Coats L, Khambadkone S, Derrick G, Mist B, Walker F, van Doorn C, Bonhoeffer P, Taylor AM. Biventricular Response After Pulmonary Valve Replacement for Right Ventricular Outflow Tract Dysfunction Is Age a Predictor of Outcome?. Circulation. 2008 Sep 30;118(14 suppl 1):S182-90.

[15] Sheehan FH, Ge S, Vick GW, Urnes K, Kerwin WS, Bolson EL, Chung T, Kovalchin JP, Sahn DJ, Jerosch-Herold M, Stolpen AH. Three-dimensional shape analysis of right ventricular remodeling in repaired tetralogy of Fallot. The American journal of cardiology. 2008 Jan 1;101(1):107-13.

[16] Leonardi B, Taylor AM, Mansi T, Voigt I, Sermesant M, Pennec X, Ayache N, Boudjemline Y, Pongiglione G. Computational modelling of the right ventricle in repaired tetralogy of Fallot: can it provide insight into patient treatment?. European Heart Journal-Cardiovascular Imaging. 2013 Apr 1;14(4):381-6.

[17] Tang D, Yang C, Geva T, Pedro J. Image-based patient-specific ventricle models with fluid–structure interaction for cardiac function assessment and surgical design optimization. Progress in pediatric cardiology. 2010 Dec 31;30(1):51-62.

[18] Trayanova NA. Whole-heart modeling applications to cardiac electrophysiology and electromechanics. Circulation research. 2011 Jan 7;108(1):113-28.

[19] Li W, Gurev V, McCulloch AD, Trayanova NA. The role of mechanoelectric feedback in vulnerability to electric shock. Progress in biophysics and molecular biology. 2008 Jul 31;97(2):461-78.

[20] Krishnamurthy A, Villongco CT, Chuang J, Frank LR, Nigam V, Belezzuoli E, Stark P, Krummen DE, Narayan S, Omens JH, McCulloch AD. Patient-specific models of cardiac biomechanics. Journal of computational physics. 2013 Jul 1;244:4-21.

[21] Kerckhoffs, Roy CP, Jeffrey H. Omens, and Andrew D. McCulloch. "A single strain-based growth law predicts concentric and eccentric cardiac growth during pressure and volume overload." *Mechanics research communications*42 (2012): 40-50.

[22] Oosterhof T, van Straten A, Vliegen HW, Meijboom FJ, van Dijk AP, Spijkerboer AM, Bouma BJ, Zwinderman AH, Hazekamp MG, de Roos A, Mulder BJ. Preoperative thresholds for pulmonary valve replacement in patients with corrected tetralogy of Fallot using cardiovascular magnetic resonance. Circulation. 2007 Jul 31;116(5):545-51.

[23] NIH Center for Integrative Biomedical Computing. Seg3D. Computer software. Seg3D: Volumetric Image Segmentation and Visualization. Vers. 2. Scientific Computing and Imaging Institute (SCI), 2015. Web.

[24] Klotz S, Hay I, Dickstein ML, Yi GH, Wang J, Maurer MS, Kass DA,

Burkhoff D. Single-beat estimation of end-diastolic pressure-volume relationship: a novel method with potential for noninvasive application. American Journal of Physiology-Heart and Circulatory Physiology. 2006 Jul 1;291(1):H403-12.

[25] Holzapfel GA, Ogden RW. Constitutive modelling of passive myocardium: a structurally based framework for material characterization. Philosophical Transactions of the Royal Society of London A: Mathematical, Physical and Engineering Sciences. 2009 Sep 13;367(1902):3445-75.

[26] Doll S, Schweizerhof K. On the development of volumetric strain energy functions. Journal of applied mechanics. 2000 Mar 1;67(1):17-21.

[27] Lumens J, Delhaas T, Kirn B, Arts T. Three-wall segment (TriSeg) model describing mechanics and hemodynamics of ventricular interaction. Annals of biomedical engineering. 2009 Nov 1;37(11):2234-55.

[28] Arts T, Delhaas T, Bovendeerd P, Verbeek X, Prinzen FW. Adaptation to mechanical load determines shape and properties of heart and circulation: the CircAdapt model. American Journal of Physiology-Heart and Circulatory Physiology. 2005 Apr 1;288(4):H1943-54.